ACS OMEGA

Open Access



http://pubs.acs.org/journal/acsodf

Article

# Influence of $TiO_2$ Particle Size on the Synthesis of Titanium−Niobium Oxides and Their Electrochemical Performance in Lithium−Ion Cells

Zhongmeng Xue, Tao Li, He Sun, Qiwei Tang, Yang Yu,* and Kunlei Zhu*

Cite This: *ACS Omega* 2025, 10, 15744−15752

Read Online

ACCESS | Metrics & More | Article Recommendations | Supporting Information

**ABSTRACT:** Developing high-performance anode materials is crucial for advancing lithium-ion batteries, particularly to meet the growing demands for higher capacity, improved safety, and enhanced rate performance in applications such as electric vehicles. In this study, we reveal the significant impact of the $TiO_2$ particle size on the synthesis and electrochemical performance of titanium−niobium oxides (TNOs). Using a high-temperature solid-phase method, we synthesized TNOs with varying compositions and sizes by reacting $TiO_2$ particles of different sizes (5−10, 10−25, 30, 60, and 100 nm) with $Nb_2O_5$ particles. Comprehensive characterization through X-ray diffraction, scanning electron microscopy, transmission electron microscopy, and electrochemical tests revealed that the TNO synthesized using 10−25 nm $TiO_2$ particles (designated as TNO4) exhibited superior electrochemical performance. TNO4 demonstrated the highest charge/discharge capacities at high current densities and exceptional cycling stability, which can be attributed to its optimal composition and particle size, both of which facilitate efficient lithium-ion diffusion and electron transport. This work not only highlights the critical role of precursor particle size in tailoring the properties of TNO anode materials but also identifies the optimal $TiO_2$ particle size for synthesizing high-performance TNOs via a simple and scalable method. Additionally, this work underscores that both the composition and the particle size of TNOs significantly affect their electrochemical performance. Our findings provide valuable insights and serve as a practical reference for the design and preparation of advanced anode materials for lithium-ion batteries.

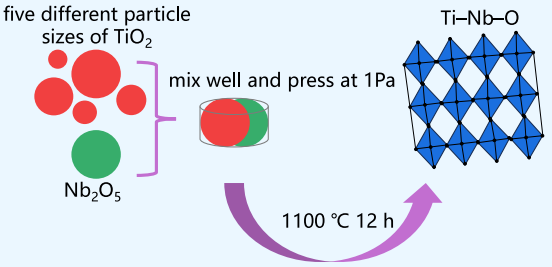


## 1. INTRODUCTION

Sony Corporation developed lithium-ion batteries (LIBs) in the 1990s. Compared to other types of batteries, LIBs offer higher energy and power density, making them widely used in portable electronic devices.[1−4] The high energy density of LIBs is due to their use of nonaqueous electrolytes, which provide a higher operating voltage (>3.2 V) compared to the aqueous electrolytes used in other systems, which typically offer lower voltages (<2 V).[5] LIBs have been widely used in consumer electronics, including portable devices, electric tools, and electric vehicles, over the past decade. However, demand is rapidly increasing for higher capacity, improved safety, better stability, and enhanced rate performance, particularly in the context of electric vehicles, where a higher capacity is crucial for longer driving ranges without compromising safety.

However, graphite-anode-based LIBs fall short of meeting the requirements for high power density and safety in practical applications. This is due to the poor alignment between the electrochemical potential of lithium-intercalated carbon anodes (Fermi energy ($E_F$) = 0.1 eV versus $Li^+/Li$) and the lowest unoccupied molecular orbital (LUMO) of organic liquid-carbonate electrolytes.[6,7] Specifically, the $E_F$ of carbonate electrolytes is about 1 eV lower than that of lithium. This discrepancy causes the electrolyte to decompose and form a solid electrolyte interface (SEI) layer, leading to initial irreversible capacity loss and poor rate performance due to the hindered transfer of $Li^+$ through the SEI layer.[8−10] Additionally, lithium dendrites tend to deposit on graphite during the fast charging and discharging processes. This can lead to internal short circuits and significantly reduce the safety of the battery.

Many studies have shown that metal oxides with stable structures can serve as effective anode materials for $Li^+$ insertion and extraction. Among them, titanium−niobium oxides can achieve higher theoretical capacities through three redox reactions: $Ti^{4+}/Ti^{3+}$, $Nb^{5+}/Nb^{4+}$, and $Nb^{4+}/Nb^{3+}$.[11−14] Most of the Ti−Nb−O groups can be represented by the chemical formula $TiNb_xO_{2+2.5x}$. In the family of titanium−niobium oxides, the inclusion of $TiNb_2O_7$ ($x$ = 2), $Ti_2Nb_{10}O_{29}$ ($x$ = 5), $TiNb_6O_{17}$ ($x$ = 6), and $TiNb_{24}O_{62}$ ($x$ = 24) corresponds to theoretical capacities of 388, 396, 397, and 401

Received: February 15, 2025
Accepted: March 20, 2025
Published: April 11, 2025





https://doi.org/10.1021/acsomega.5c01447
*ACS Omega* 2025, 10, 15744−15752

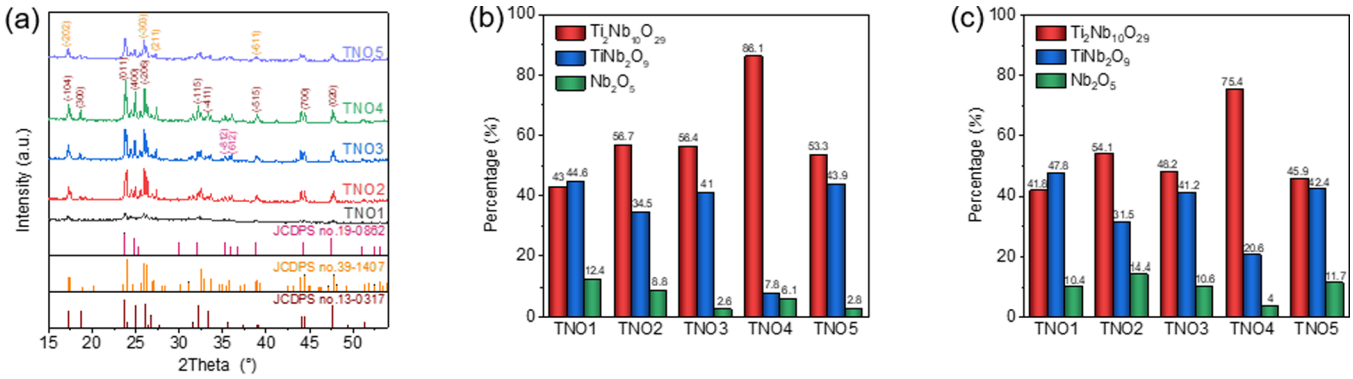


**Figure 1.** (a) XRD patterns and composition percentages calculated using XRD (b) peak area and (c) peak intensity of the as-prepared titanium−niobium oxides.

mAh $g^{-1}$, respectively.[15−18] Moreover, the stable Wadsley-Roth shear structure of $TiNb_xO_{2+2.5x}$ contributes to its good cycling stability.[19−21] Furthermore, similar to $Nb_2O_5$ electrodes, the $TiNb_xO_{2+2.5x}$ family has a high operating voltage of approximately 1.0−2.0 V (versus $Li^+/Li$),[22−24] which aligns well with the LUMO of organic liquid-carbonate electrolytes.[25−27] The formation of lithium dendrites can be avoided, thereby ensuring the safety of the battery.[20,28]

In 2011, Goodenough's group first reported on the use of $TiNb_2O_7$ as a negative electrode material for lithium batteries.[29,30] It undergoes a 5-electron transfer process during lithium ion deintercalation, corresponding to multiple redox reactions: ($Ti^{4+}/Ti^{3+}$, $Nb^{5+}/Nb^{4+}$, and $Nb^{4+}/Nb^{3+}$),[12,31] and exhibits excellent electrochemical performance. Following the initial report, several other research groups also studied $TiNb_2O_7$. In addition to the extensively studied $TiNb_2O_7$, other Ti−Nb−O electrodes such as $Ti_2Nb_{10}O_{29}$, $TiNb_6O_{17}$, and $TiNb_{24}O_{62}$ have also garnered significant interest in energy storage systems.[15,17,28] According to the theoretical capacity calculation formula, the theoretical capacity of $TiNb_xO_{2+2.5x}$ increases with an increasing $x$ value. These $TiNb_xO_{2+2.5x}$ ($x > 2$) compounds, with higher theoretical capacity, have attracted increasing attention.

$Ti_2Nb_{10}O_{29}$, with its high theoretical specific capacity (396 mAh $g^{-1}$) and suitable working potential, is regarded as one of the most promising negative electrode materials for LIBs.[32,33] In 2012, Chen group published results on the electrochemical deintercalation of lithium from $Ti_2Nb_{10}O_{29}$, demonstrating that its charge−discharge mechanism is similar to that of $TiNb_2O_7$.[34]

Ti−Nb−O materials are typically prepared using various methods, including the solvothermal method,[6,20,33] sol−gel method,[35,36] electrostatic spinning method,[37] polypyrrole-chemical vapor deposition method,[38] and high-temperature solid-phase method.[39,40] Among these methods, solvothermal, sol−gel, electrostatic spinning, and polypyrrole-chemical vapor deposition techniques are time-consuming and involve a complex process. In contrast, the high-temperature solid-phase method offers advantages such as low cost, high yield, and a simpler process, making it the primary method for producing electrode materials for LIBs. The synthesis method involves transferring the solid precursors to a heating furnace after preliminary grinding and mixing. The desired materials are then obtained through high-temperature calcination, crystal bonding, and cooling under an appropriate atmosphere. The titanium−niobium oxides are typically synthesized through the high-temperature calcination of a mixture of $TiO_2$ and $Nb_2O_5$. However, the electrochemical performance of materials prepared by the high-temperature solid-phase method is relatively poor overall[39] and may be influenced by properties of titanium−niobium oxide materials, such as particle size and composition. Thus, it is important to synthesize titanium−niobium oxide materials with varying compositions and particle sizes to explore their electrochemical performance, establishing the relationship between these properties and the electrochemical performance of titanium−niobium oxide materials.

In this work, we synthesized titanium−niobium oxides with varying compositions and particle sizes by reacting five different particle sizes of $TiO_2$ with $Nb_2O_5$ using a high-temperature solid-phase method. The synthesis of $Ti_2Nb_{10}O_{29}$ reported in the current literature did not explore the influence of particle size of the raw materials (e.g., $TiO_2$). X-ray diffraction (XRD), scanning electron microscopy (SEM), and transmission electron microscopy (TEM) were conducted to characterize the as-prepared Ti−Nb−O materials. Furthermore, we performed electrochemical tests, including galvanostatic tests, cyclic voltammetry (CV), and electrochemical impedance spectroscopy (EIS) measurements, to study the electrochemical performance and related storage mechanism of these as-prepared titanium−niobium oxides. The results demonstrate that TNO4, synthesized using 10−25 nm $TiO_2$, exhibits the highest percentage of $Ti_2Nb_{10}O_{29}$, the smallest particle size, and the best cycling performance at 1 C (1 C = 396 mA $g^{-1}$). In contrast, TNO1, synthesized using 100 nm $TiO_2$ has the highest percentage of $TiNb_2O_7$, the largest particle size, and the highest discharge capacity at 0.1 C.

## 2. EXPERIMENTAL SECTION

**2.1. Material Synthesis.** Using the high-temperature solid-phase synthesis method, $TiO_2$ of different particle sizes (100, 60, 30, 10−25, and 5−10 nm, respectively) were purchased and uniformly mixed with $Nb_2O_5$ particles. The mixture was then placed in a mold and pressed at 1 MPa. The mixture of $TiO_2$ and $Nb_2O_5$ was placed in a crucible and then heated in a muffle furnace at 1100 °C for 12 h. The as-prepared titanium−niobium oxides were designated as TNO1, TNO2, TNO3, TNO4, and TNO5, respectively.

**2.2. Materials Characterization.** SEM images were obtained by using a Hitachi S-4800 microscope. TEM images were captured with a JEOL JEM-2100F microscope. XRD


https://doi.org/10.1021/acsomega.5c01447
ACS Omega 2025, 10, 15744−15752

patterns were collected on a Rigaku *D*/max 2500 PC diffractometer.

All electrochemical tests were performed at room temperature by using CR2032 coin cells. The anode electrode was prepared by mixing the active material, acetylene black, and poly(tetrafluoroethylene) in a weight ratio of 80:10:10. The mass loading of each electrode is ∼2 mg $cm^{-2}$. Metallic lithium foil served as both the reference and counter electrodes. The electrolyte was a solution of 1 M $LiPF_6$ using a mixture of ethylene carbonate, diethyl carbonate, and dimethyl carbonate (1:1:1 by volume) as the solvent. Constant current charge−discharge measurements were conducted by using a LAND CT2001A battery testing system. The test voltage window was set to 1−3 V versus $Li^+/Li$. CV measurements were conducted at a scan rate of 0.2 mV $s^{-1}$ by using a CHI 760E electrochemical workstation. EIS measurements were performed using a CHI 760E electrochemical workstation with a perturbation of 5 mV.

## 3. RESULTS AND DISCUSSION

As revealed by XRD patterns (Figure 1a), the results show that the as-prepared titanium−niobium oxides have multiple phases, consisting of $Ti_2Nb_{10}O_{29}$ (JCPDS card no. 13-0317), $TiNb_2O_7$ (JCPDS card no. 39-1407), and a small amount of $Nb_2O_5$ (JCPDS card no. 19−0862). Among these, the peaks of TNO4 are high and narrow, indicating the best crystallinity. The typical diffraction peaks of TNO4 appear at 2$\theta$ values of 17.3, 18.7, 23.8, 24.9, 26.1, 32.2, 33.3, 35.6, 38.9, 44.4, and 47.6° corresponding to the (−104), (300), (011), (400), (−206), (−115), (−411), (206), (−515), (700), and (020) crystal planes of $Ti_2Nb_{10}O_{29}$.[41] Additionally, the peak at 26.9° corresponds to the (221) crystal plane of $TiNb_2O_7$, while the peaks at 35.3 and 35.9° correspond to the (−812) and (612) crystal planes of $Nb_2O_5$,[42] respectively.

In addition, the compositions of these samples were analyzed based on XRD results. The compositions of electrochemical materials directly affect their charge storage capacity and electrochemical behavior, which in turn influence the overall performance. The composition percentages of each sample were calculated based on peak intensity and peak area, respectively. The peak areas (Figure 1b, Table 1) and peak intensities (Figure 1c, Table 2) were calculated, plotted, and tabulated to summarize the data. It can be clearly seen that the TNO1 sample has the highest percentage of $TiNb_2O_7$, whereas the main composition for the TNO2−TNO5 samples is $Ti_2Nb_{10}O_{29}$. For TNO1, it has the highest percentage of $TiNb_2O_7$: $TiNb_2O_7$ accounts for 44.6% based on XRD peak areas and 47.8% based on the XRD peak intensity. $Ti_2Nb_{10}O_{29}$ accounts for 43 and 41.8%, respectively, while $Nb_2O_5$ accounts for 12.4 and 10.4%, respectively. For TNO4, it has the highest percentage of $Ti_2Nb_{10}O_{29}$: $Ti_2Nb_{10}O_{29}$ accounts for 86.1% based on XRD peak areas and 75.4% based on the XRD peak intensity. $TiNb_2O_7$ accounts for 7.8 and 20.6%, respectively, while $Nb_2O_5$ accounts for 6.1 and 4%, respectively. Moreover, the results of the composition of the phases were further determined by Rietveld refinements (Figure S1 and Table S1), and the trends were consistent with the above results. Overall, that TNO4, synthesized using 10−25 nm $TiO_2$, exhibits the highest percentage of $Ti_2Nb_{10}O_{29}$, while, TNO1, synthesized using 100 nm $TiO_2$ has the highest percentage of $TiNb_2O_7$.

Based on the experimental results, it is shown that $TiO_2$ with a large particle size is more likely to generate $TiNb_2O_7$.[43] While $TiO_2$ with a small particle size is more likely to generate $Ti_2Nb_{10}O_{29}$. Smaller particle sizes of $TiO_2$ are able to reach the desired degree of reaction in a shorter period of time, thus increasing the yield of $Ti_2Nb_{10}O_{29}$.

Figure 2 shows SEM images of TNO1 (Figure 2a−c), TNO2 (Figure 2d−f), TNO3 (Figure 2g−i), TNO4 (Figure 2j−l), and TNO5 (Figure 2m−o), respectively. It can be observed that titanium−niobium oxides exhibit a relatively similar particle morphology consisting of irregular block-shaped particles with ample gaps between them. This morphology is advantageous for facilitating the entry of the electrolyte. The particle sizes of titanium−niobium oxides

**Table 1. Composition Percentages of the As-Prepared Titanium−Niobium Oxides Were Determined Based on XRD Peak Areas**

| | TNO1 | TNO2 | TNO3 | TNO4 | TNO5 |
|---|---|---|---|---|---|
| $Ti_2Nb_{10}O_{29}$ | 43% | 56.7% | 56.4% | 86.1% | 53.3% |
| $TiNb_2O_7$ | 44.6% | 34.5% | 41% | 7.8% | 43.9% |
| $Nb_2O_5$ | 12.4% | 8.8% | 2.6% | 6.1% | 2.8% |

**Table 2. Composition Percentages of the As-Prepared Ti−Nb−O Samples Were Determined Based on XRD Peak Intensities**

| | TNO1 | TNO2 | TNO3 | TNO4 | TNO5 |
|---|---|---|---|---|---|
| $Ti_2Nb_{10}O_{29}$ | 41.8% | 54.1% | 48.2% | 75.4% | 45.9% |
| $TiNb_2O_7$ | 47.8% | 31.5% | 41.2% | 20.6% | 42.9% |
| $Nb_2O_5$ | 10.4% | 14.4% | 10.6% | 4% | 11.7% |

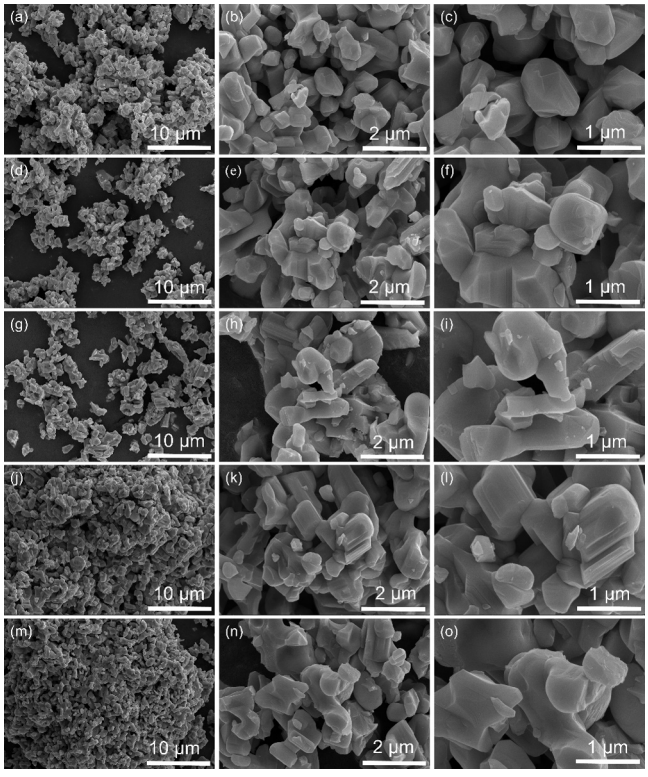


**Figure 2.** SEM images of titanium−niobium oxides shown as follows: (a−c) TNO1, (d−f) TNO2, (g−i) TNO3, (j−l) TNO4, and (m−o) TNO5.



https://doi.org/10.1021/acsomega.5c01447
ACS Omega 2025, 10, 15744−15752

prepared using different $TiO_2$ particle sizes also vary. Among the five samples (TNO1−TNO5), the average particle sizes are 1.09, 1.03, 1.06, 0.94, and 1.00 $\mu$m, respectively. Among them, TNO4, made using $TiO_2$ with a particle size of 10−25 nm, has the smallest particle size at 0.94 $\mu$m.

Further, SEM measurements were performed on the cycled TNO4 electrode, as shown in Figure S5. It can be observed that the structure of the postcycled TNO4 is not much different from that of the pristine TNO4, and the average particle size of the postcycled TNO4 measured by the SEM results is 0.95 $\mu$m, which is basically the same as the average particle size of the pristine TNO4.

TEM measurements were further performed to reveal the structures of TNO4, as shown in Figure 3. TNO4 is composed

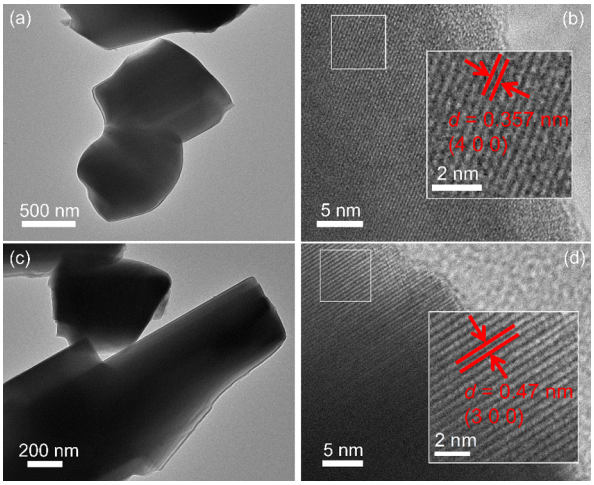


**Figure 3.** (a, c) TEM images of TNO4. (b, d) HRTEM images of TNO4.

of many irregular blocky structures (Figure 3a,c), which agrees with the SEM results. The high-resolution TEM (HRTEM) image of a TNO4 nanocrystal presents a (400) plane with a lattice spacing of 0.357 nm (Figure 3b)[7] and (300) with a lattice spacing of 0.47 nm (Figure 3d),[6] indicating that the major phase of TNO4 is $Ti_2Nb_{10}O_{29}$. In addition, we performed TEM measurements on a circulated TNO4 electrode (Figure S4). The HRTEM image of the cycled TNO4 electrode nanocrystal presents a (011) plane with a lattice spacing of 0.37 nm (Figure S4a).[12] TNO4 is composed of many irregular blocky structures (Figure S4b), which agrees with the precycled TNO4's result.

The crystal structure of the $Ti_2Nb_{10}O_{29}$ compound is $ReO_3$ type, and the space group is $A2/m$. The $ReO_3$ structure can be evolved from the $ABO_3$ perovskite structure, in which the A cation is replaced by a vacancy. The host can be used as a storage material because of its potential to absorb small cations such as $Li^+$. The $Ti_2Nb_{10}O_{29}$ compound, whose structure is composed of crystal shear planes along the (010) direction, can be described separately as AB.[34]

$TiNb_2O_7$ has a monoclinic layered structure with a space group of $C2/m$. Each layer has a different arrangement of atoms in the (010) direction than the adjacent layer but is the same as the next, forming an A-B-A type structure within the unit cell. Two titanium atoms symmetrically distributed near the center and a third titanium atom near the $c$-axis are the most favorable energy configurations. Chen's group used first-principles calculations and spherical aberration-corrected scanning transmission electron microscopy to study possible lithium storage sites. The results show that the lithium ions are stored in the (001) lattice plane of $TiNb_2O_7$, and the lattice constant changes when the lithium is inserted.[44]

For $TiNb_2O_7$ and $Ti_2Nb_{10}O_{29}$, during the discharge process (lithium intercalation), lithium ions enter the framework, causing slight changes in the material's oxidation state (mainly affecting titanium and niobium atoms). Deintercalation during charge involves the reverse of this process, where lithium ions leave the structure, leading to the oxidation of titanium or niobium atoms in the framework and thus allowing the deintercalation of lithium ions. This is typically achieved by applying an external voltage that forces Li ions to migrate from the material's bulk structure to the electrolyte, where they become solvated and then can move to the anode or cathode depending on the battery's operational cycle. The corresponding equations are as follows:

$$x\mathrm{Li}^+ + x\mathrm{e}^- + \mathrm{TiNb_2O_7} \rightleftharpoons \mathrm{Li}_x\mathrm{TiNb_2O_7} \quad (1)$$

$$x\mathrm{Li}^+ + x\mathrm{e}^- + \mathrm{Ti_2Nb_{10}O_{29}} \rightleftharpoons \mathrm{Li}_x\mathrm{Ti_2Nb_{10}O_{29}} \quad (2)$$

To gain deeper insights into the redox reactions at the electrodes, CV measurements were conducted for TNO1, TNO2, TNO3, TNO4, and TNO5, each assembled in half-cells, over a voltage range of 1−3 V at a scan rate of 0.2 mV $s^{-1}$ (Figure 4a−e). These samples exhibit similar redox peaks in the CV curves. Taking Figure 4a as an example, during initial charging and discharging, the shift of $Ti^{4+}$ to $Ti^{3+}$ results in broad redox peaks at 1.83 V. In addition, a pair of sharp cathodic/anodic peaks are observed at ∼1.57 and 1.71 V, and the first loop CV (Figure S2) cathode/anode peak is ∼1.48 and 1.71 V, which could be attributed to the $Nb^{5+}/Nb^{4+}$ transition. It can be clearly seen that the CV curve is shifted to the right, which can be regarded as the activation process of the electrode. While the fluctuation at 1.42 V is caused by the $Nb^{4+}/Nb^{3+}$ redox pair.[33,45,46] Subsequently, the second and third cycles of TNO1−TNO5 exhibit slightly different CV profiles compared to the first cycle. This variation can be attributed to $Li^+$ insertion and changes in the electronic structure resulting from Nb(Ti)−O octahedral distortion during irreversible lithiation.[37]

Although the CV curves of the five titanium−niobium oxides follow the same general trend (Figure 4), the differing compositions of the samples lead to distinct features. TNO1 is primarily composed of $TiNb_2O_7$, while TNO2−TNO5 is dominated by $Ti_2Nb_{10}O_{29}$ (Figure 1, Tables 1 and 2). The main cathodic/anodic peaks of TNO2−TNO5 are observed at 1.53/1.76, 1.55/1.77, 1.56/1.77, and 1.56/1.79 V, respectively, as shown in Figure 4e. Based on the calculations, the voltage difference ($\Delta E$) of the redox reaction for each material is determined to be 0.15, 0.23, 0.22, 0.21, and 0.23 V, respectively. Among them, TNO1 has the smallest $\Delta E$, indicating faster kinetics at a low scanning rate, which leads to a higher peak in the corresponding CV curve (Figure 4f). The smallest redox voltage difference for TNO1 may be attributed to the composition of the material. Compared with TNO1, TNO2, TNO3, and TNO5, the curves of TNO4 present a relatively high consistency after the first cycle, indicating superior electrochemical stability.

Figure 5a−d shows the relationship between voltage and capacity for TNO1, TNO2, TNO3, TNO4, and TNO5 in the voltage range of 1−3 V at 0.2 and 1 C. For TNO1−TNO5, the discharge curves can be categorized into three regions. The


https://doi.org/10.1021/acsomega.5c01447
ACS Omega 2025, 10, 15744−15752

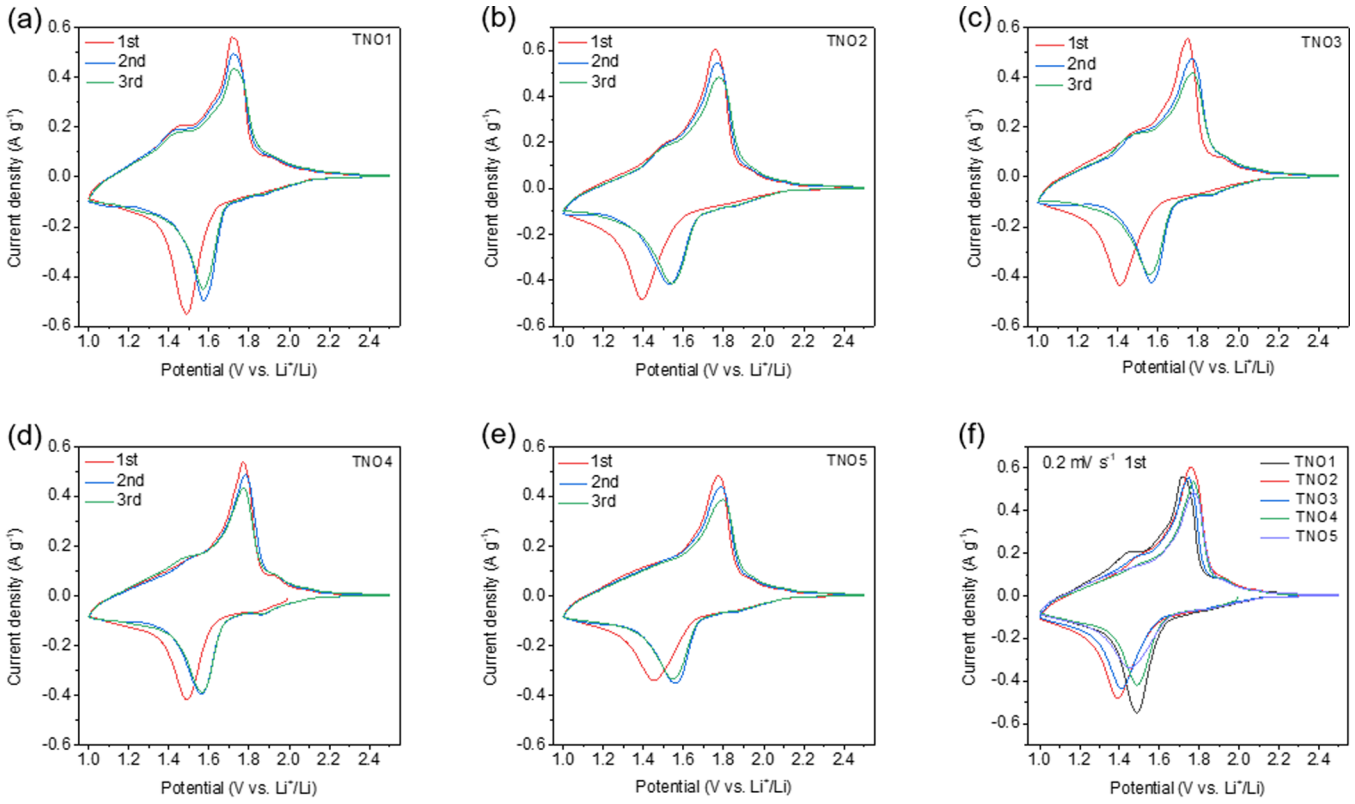


**Figure 4.** CV curves for the initial three cycles at a scan rate of 0.2 mV $s^{-1}$ for (a) TNO1, (b) TNO2, (c) TNO3, (d) TNO4, and (e) TNO5. (f) CV curves for the initial first cycle at a scan rate of 0.2 mV $s^{-1}$ for the five titanium−niobium oxides.

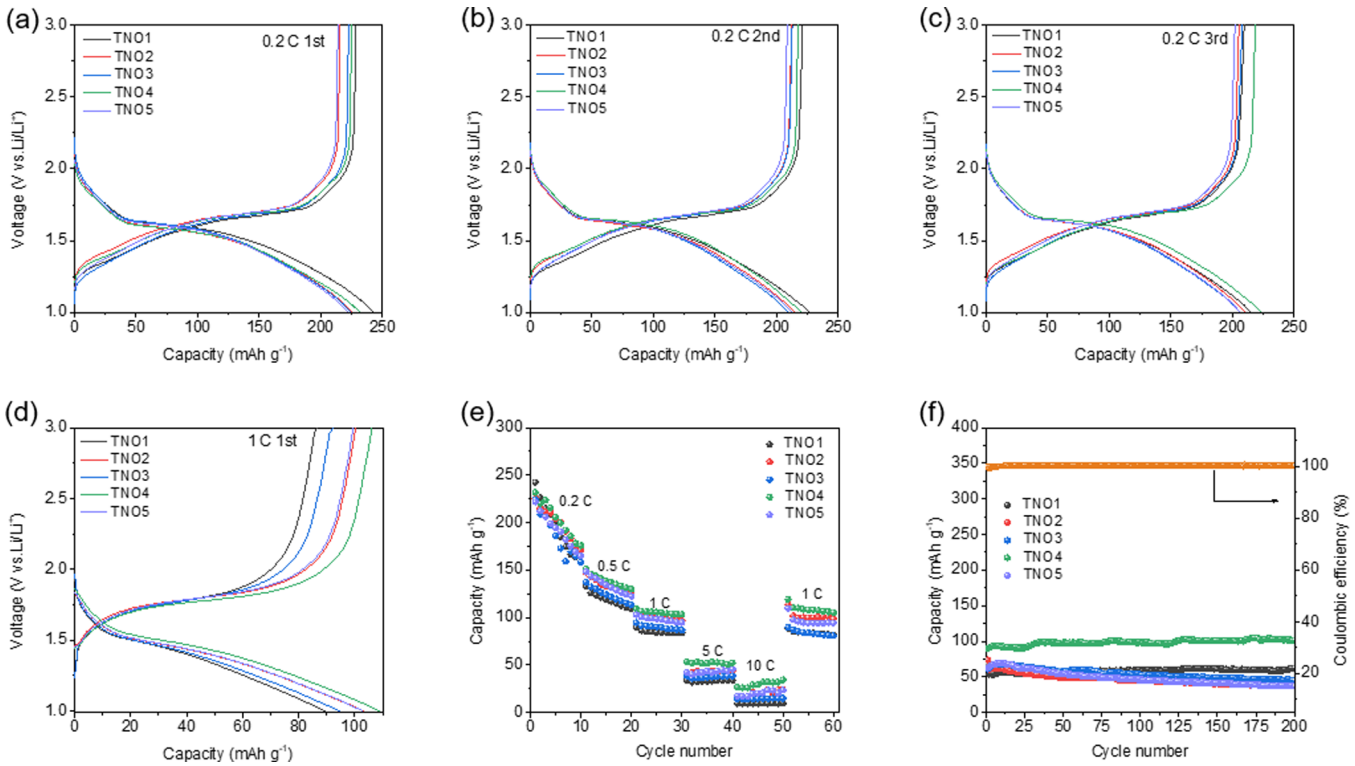


**Figure 5.** (a) First, (b) second, and (c) third galvanostatic discharge/charge curves of the five titanium−niobium oxides at 0.2 C. (d) First galvanostatic discharge/charge curves of the five titanium−niobium oxides at 1 C. (e) Rate capacity curves of the five titanium−niobium oxides at various current densities. (f) Cycling performance of the five titanium−niobium oxides over 200 cycles at 1 C.

first region is a sharp voltage drop from the open-circuit voltage to ∼1.60 V versus $Li^+$ /Li, corresponding to the $Ti^{4+}$/$Ti^{3+}$ redox reaction. The second region presents a plateau region around 1.60−1.50 V, associated with the successive



https://doi.org/10.1021/acsomega.5c01447
ACS Omega 2025, 10, 15744−15752

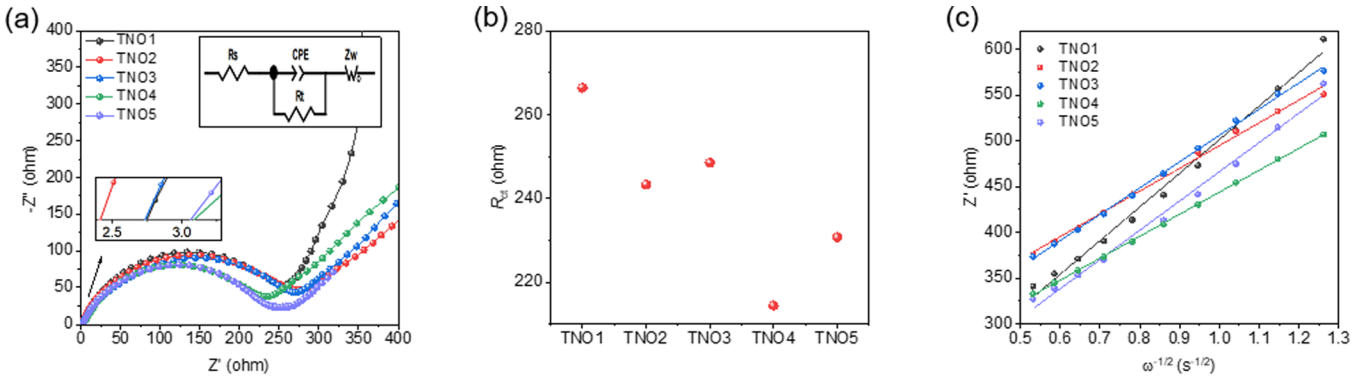


**Figure 6.** (a) EIS spectra, (b) $R_{ct}$ values, and (c) fitting curves of the Warburg factor $\sigma$ using the real axis $Z'$ and frequency $\omega$ for the five titanium−niobium oxides before cycling tests.

lithium insertions involving the $Nb^{5+}$ /$Nb^{4+}$ reaction during the two-phase transition. The final region, between 1.00−1.50 V, reflects solid-solution lithium insertion behavior, corresponding to the $Nb^{4+}$/$Nb^{3+}$ redox reaction.[23,33,47] Similarly, three distinct regions emerge during the subsequent charging process.

Figure 5a presents the galvanostatic discharge/charge curves during the first cycle at 0.2 C. The charge/discharge capacities for TNO1−TNO5 are 228.5/242.5, 215.4/225.3, 222.4/224.2, 224.6/231.7, and 213.7/221.9 mAh $g^{-1}$, respectively. Figure 5b shows the galvanostatic curves for the second cycle at 0.2 C, with charge/discharge capacities of 221.0/226.4, 211.9/215.0, 212.4/208.8, 217.1/220.0, and 208.4/212.2 mAh $g^{-1}$, respectively. Figure 5c illustrates the galvanostatic discharge/charge curves for the cycle at 0.2 C, where the capacities for TNO1−TNO5 are 209.3/215.0, 205.5/211.6, 207.6/206.2, 218.2/223.8, and 201.8/206.1 mAh $g^{-1}$, respectively. Figure 5d shows the curves during the first cycle at 1 C, with charge/discharge capacities of 125.9/132.7, 141.9/147.7, 133.2/137.4, 145.5/151.4, and 142.4/148.3 mAh $g^{-1}$ for TNO1−TNO5, respectively. Despite having the largest particle size, TNO1 exhibits the highest capacity during the first and second charge/discharge cycles at a low current density of 0.2 C (Figure 5a,b), consistent with the above CV results. The slightly higher initial capacity of TNO1 at 0.2 C may be attributed to its composition, which is predominantly $TiNb_2O_7$. However, its lower purity and larger particle size led to the most significant capacity decline during the test, with the battery's capacity continuing to decay to the lowest level (Figure 5c). Furthermore, $TiNb_2O_7$-dominated TNO1 shows the lowest charge/discharge capacity at a high current density of 1 C, while $Ti_2Nb_{10}O_{29}$-dominated TNO4 exhibits the highest. This indicates that $Ti_2Nb_{10}O_{29}$ may have faster reaction kinetics than $TiNb_2O_7$ at higher current densities, a conclusion further supported by the subsequent rate capability test (Figure 5e).

Figure 5e shows the rate capacities of TNO1−TNO5. At the same rate (0.2, 0.5, 1, 5, and 10 C), the average charge/discharge capacities for TNO4 are 197.5/202.9, 136.7/138.7, 104.7/105.4, 52.5/52.3, and 31.0/29.9 mAh $g^{-1}$, respectively. For TNO1, they are 187.80/193.85, 116.99/118.75, 84.4/85.0, 33.2/33.2, and 10.1/9.5 mAh $g^{-1}$. For TNO2, they are 175.7/180.7, 131.8/133.9, 98.6/99.3, 43.2/42.7, and 21.2/19.9 mAh $g^{-1}$. TNO3 averages 186.23/184.7, 123.6/123.8, 89.7/89.9, 37.3/37.4, and 15.1/14.4 mAh $g^{-1}$. For TNO5, the values are 187.0/191.6, 131.8/134.0, 97.3/98.2, 43.3/43.0, and 22.0/20.3 mAh $g^{-1}$. Overall, TNO4 consistently shows higher average charge/discharge capacities than other materials, particularly at the high rate of 10 C.

Additionally, the cycling performance of each electrode was tested for 200 cycles at 1 C, as shown in Figure 5f. TNO4 demonstrates an initial reversible capacity of 89.7 mAh $g^{-1}$ with an efficiency of approximately 99.7%. After 200 cycles, the reversible capacity gradually increases to 101.7 mAh $g^{-1}$ with an efficiency of nearly 100%. In contrast, the initial reversible capacities of TNO1, TNO2, TNO3, and TNO5 are 67.3, 74.1, 60.6, and 63.1 mAh $g^{-1}$, respectively, which decrease to 62.7, 39.6, 45.5, and 37.3 mAh $g^{-1}$ after 200 cycles. We selected TNO1 and TNO4 to assemble the battery for 1000 long cycles for comparison (Figure S3), and the results show that the first charge and discharge capacity of TNO4 is 100.9/98.5 mAh $g^{-1}$, and TNO1 is 72.3/62.2 mAh $g^{-1}$. In the first circle, the charge and discharge capacity of TNO1 decreases rapidly; after 1000 cycles, the charge and discharge capacity of TNO1 is 18.7/18.6 mAh $g^{-1}$, and the charge and discharge capacity of TNO4 is 25.8/25.8 mAh $g^{-1}$. This highlights that TNO4 not only has a much higher capacity than those of the other four materials but also demonstrates superior cycling stability. The enhanced rate capability and cycling performance of TNO4 can be attributed to its purity (the highest percentage of $Ti_2Nb_{10}O_{29}$, which has a high theoretical capacity) and its smallest particle size.

We compare the results of this work with published work (Table S2), and the results of the present work show an intermediate level in comparison. Specifically, our battery capacity is slightly inferior for some studies compared to others but shows relatively good performance compared to some fundamental research work.

EIS measurements reveal the reaction kinetics of these titanium−niobium oxides before cycling (Figure 6a). The EIS spectra are fitted based on the equivalent circuit (inset), where $R_s$ is the series resistance of the electrode, separator, and electrolyte, $R_t$ is the transfer resistance of the material, CPE represents the double-layer capacitance, and $Z_w$ is the Warburg impedance.[48,49] The fitted values of $R_{ct}$ are shown in Figure 6b. TNO4 exhibits a smaller $R_{ct}$ value both before and after testing, which can be attributed to its higher conductivity and faster electrochemical reaction kinetics.

The diffusion coefficients of lithium ions within the electrodes were calculated by using the EIS method.

$$Z' = R_s + R_{ct} + \sigma\omega^{-1/2} \quad (3)$$



https://doi.org/10.1021/acsomega.5c01447
ACS Omega 2025, 10, 15744−15752

Table 3. $D_{Li^+}$ Values of the Five Titanium−Niobium Oxides Based on EIS Spectra

| | TNO1 | TNO2 | TNO3 | TNO4 | TNO5 |
|---|---|---|---|---|---|
| $D_{Li^+}$ ($cm^2\ s^{-1}$) | $4.10 \times 10^{-16}$ | $8.96 \times 10^{-16}$ | $6.71 \times 10^{-16}$ | $9.61 \times 10^{-16}$ | $5.42 \times 10^{-16}$ |

$$D_{Li^+} = \frac{R^2T^2}{2n^2A^2F^2C^2\sigma^2} \quad (4)$$

Here, $\omega$ is the angular frequency, and $\sigma$ represents the slope of $Z'$ versus $\omega^{-1/2}$ plots in the low-frequency region. $R$ is the gas constant, $T$ denotes the absolute temperature, $n$ represents the number of electrons transferred during oxidation, $A$ refers to the electrode surface area, $F$ is the Faraday constant, and $C$ represents the concentration of lithium ions. Values of $\sigma$ can be obtained by fitting the $Z'$ versus $\omega^{-1/2}$ plots displayed in Figure 6c. The lithium-ion diffusion coefficient ($D_{Li^+}$) values calculated using eqs 3 and 4 are shown in Table 3. The lithium-ion diffusion coefficient of the TNO4 sample ($9.6 \times 10^{-16}$ $cm^2$ $s^{-1}$) is significantly higher compared to other samples, indicating superior ionic conductivity in TNO4. The enhanced ionic conductivity can be attributed to TNO4's stronger adsorption capacity for $Li^+$ and its rapid electron transfer reactions, both of which contribute to its excellent electrochemical performance.

## 4. CONCLUSIONS

In this study, we synthesized titanium−niobium oxide materials using a high-temperature solid-phase method by reacting $TiO_2$ with $Nb_2O_5$ at 1100 °C for 12 h. $TiO_2$ particles of varying particle sizes (100, 60, 30, 10−25, and 5−10 nm) were used in the synthesis. By adjusting the particle size of $TiO_2$, we explored its influence on the composition, particle size, and electrochemical properties of the resulting titanium−niobium oxides. Our findings demonstrate that the particle size of $TiO_2$ has a significant effect on the composition and electrochemical performance of the synthesized materials. The sample prepared with 100 nm $TiO_2$ (TNO1) exhibited distinct characteristics compared to the others, including a higher proportion of $TiNb_2O_7$, larger particle size, and higher charge−discharge capacities at low current densities. However, TNO1 also showed poor cycling stability, which can be attributed to its lower purity and larger particle size. In contrast, the samples prepared with smaller $TiO_2$ particles (TNO2−TNO4), which were predominantly composed of $Ti_2Nb_{10}O_{29}$, exhibited smaller particle sizes, higher charge−discharge capacities at high current densities, and superior cycling performance. Notably, the TNO4 sample, synthesized using 10−25 nm $TiO_2$, demonstrated the most optimal electrochemical properties, making it the most promising candidate among the materials tested. This work identifies 10−25 nm $TiO_2$ as the optimal particle size for synthesizing $Ti_2Nb_{10}O_{29}$ via a simple high-temperature solid-phase method. The findings provide valuable insights and serve as a reference for the preparation of high-performance titanium−niobium oxide materials, contributing to the advancement of efficient anode materials for LIBs.

## ■ ASSOCIATED CONTENT

### Supporting Information

The Supporting Information is available free of charge at https://pubs.acs.org/doi/10.1021/acsomega.5c01447.

Rietveld XRD patterns of TNO1 sample, TNO2 sample, TNO3 sample, TNO4 sample, and TNO5 sample; composition percentage of the as-prepared Ti−Nb−O samples determined based on Rietveld refinements results; CV curves for the initial first cycle at a scan rate of 0.2 mV $s^{-1}$ for the TNO1; cycling performance of the TNO1and TNO2 over 1000 cycles at 5 C; HRTEM images of the cycled TNO4 and TEM images of the cycled TNO4; SEM image of the cycled TNO4 and enlarged SEM image of the cycled TNO4; and comparison of results with previous literature (PDF)

## ■ AUTHOR INFORMATION


### Corresponding Authors

**Yang Yu** − *School of Chemistry and Chemical Engineering, Qufu Normal University, Qufu, Shandong 273165, P. R. China*; Email: yangyuqfnu@qfnu.edu.cn

**Kunlei Zhu** − *School of Chemistry and Chemical Engineering, Qufu Normal University, Qufu, Shandong 273165, P. R. China*; orcid.org/0000-0001-7823-7479; Email: zhyq9188@126.com, zhukunlei@qfnu.edu.cn

### Authors

**Zhongmeng Xue** − *School of Chemistry and Chemical Engineering, Qufu Normal University, Qufu, Shandong 273165, P. R. China*

**Tao Li** − *School of Chemistry and Chemical Engineering, Qufu Normal University, Qufu, Shandong 273165, P. R. China*

**He Sun** − *School of Energy and Mechanical Engineering, Dezhou University, Dezhou 253023, China*

**Qiwei Tang** − *School of Energy and Mechanical Engineering, Dezhou University, Dezhou 253023, China*

Complete contact information is available at: https://pubs.acs.org/10.1021/acsomega.5c01447


### Notes

The authors declare no competing financial interest.

## ■ ACKNOWLEDGMENTS

The research was financially supported by the Scientific Research Foundation of Qufu Normal University (No. 613701), the Natural Science Foundation of Shandong Province (No. ZR2023MB062), and the National Natural Science Foundation of China (No. 52272041).

## ■ REFERENCES

(1) Placke, T.; Kloepsch, R.; Dühnen, S.; Winter, M. Lithium ion, lithium metal, and alternative rechargeable battery technologies: the odyssey for high energy density. *J. Solid State Electrochem.* **2017**, *21* (7), 1939−1964.

(2) Winslow, K. M.; Laux, S. J.; Townsend, T. G. A review on the growing concern and potential management strategies of waste lithium-ion batteries. *Resources, Conservation and Recycling* **2018**, *129*, 263−277.

(3) Wu, W.; Liu, M.; Pei, Y.; Li, W.; Lin, W.; Huang, Q.; Wang, M.; Yang, H.; Deng, L.; Yao, L.; Zheng, Z. Unprecedented Superhigh-Rate and Ultrastable Anode for High-Power Battery via Cationic Disordering. *Adv. Energy Mater.* **2022**, *12* (30), No. 2201130.

(4) Liu, J.; Jing, P.; Zheng, L.; Guo, N.; Liu, C.; Wang, H. Diffusion tunnel shortening and Oxygen-Vacancy boosting high rate and stable

lithium ion storage of crystallographic self-healed $Ti_2Nb_{10}O_{29}$ anode. *Chemical Engineering Journal* **2024**, *482*, No. 148866.
(5) Xia, L.; Miao, H.; Zhang, C.; Chen, G. Z.; Yuan, J. Review—recent advances in non-aqueous liquid electrolytes containing fluorinated compounds for high energy density lithium-ion batteries. *Energy Storage Materials* **2021**, *38*, 542−570.
(6) Lou, S.; Cheng, X.; Gao, J.; Li, Q.; Wang, L.; Cao, Y.; Ma, Y.; Zuo, P.; Gao, Y.; Du, C.; Huo, H.; Yin, G. Pseudocapacitive $Li^+$ intercalation in porous $Ti_2Nb_{10}O_{29}$ nanospheres enables ultra-fast lithium storage. *Energy Storage Materials* **2018**, *11*, 57−66.
(7) Deng, S.; Zhu, H.; Liu, B.; Yang, L.; Wang, X.; Shen, S.; Zhang, Y.; Wang, J.; Ai, C.; Ren, Y.; Liu, Q.; Lin, S.; Lu, Y.; Pan, G.; Wu, J.; Xia, X.; Tu, J. Synergy of Ion Doping and Spiral Array Architecture on $Ti_2Nb_{10}O_{29}$: A New Way to Achieve High-Power Electrodes. *Adv. Funct. Mater.* **2020**, *30* (25), No. 2002665.
(8) Intan, N. N.; Pfaendtner, J. Effect of Fluoroethylene Carbonate Additives on the Initial Formation of the Solid Electrolyte Interphase on an Oxygen-Functionalized Graphitic Anode in Lithium-Ion Batteries. *ACS Appl. Mater. Interfaces* **2021**, *13* (7), 8169−8180.
(9) Yan, C.; Xu, R.; Xiao, Y.; Ding, J.; Xu, L.; Li, B.; Huang, J. Toward Critical Electrode/Electrolyte Interfaces in Rechargeable Batteries. *Adv. Funct. Mater.* **2020**, *30* (23), No. 1909887.
(10) Bak, S.-E; Chung, W.; Abbas, M. A.; Bang, J. H. Amorphization-Driven Lithium Ion Storage Mechanism Change for Anomalous Capacity Enhancement. *ACS Appl. Mater. Interfaces* **2023**, *15* (29), 34874−34882.
(11) Wang, H.; Qian, R.; Cheng, Y.; Wu, H.-H.; Wu, X.; Pan, K.; Zhang, Q. Micro/nanostructured $TiNb_2O_7$-related electrode materials for high-performance electrochemical energy storage: recent advances and future prospects. *Journal of Materials Chemistry A* **2020**, *8* (36), 18425−18463.
(12) Tang, Y.; Deng, S.; Shi, S.; Wu, L.; Wang, G.; Pan, G.; Lin, S.; Xia, X. Ultrafast and durable lithium ion storage enabled by intertwined carbon nanofiber/$Ti_2Nb_{10}O_{29}$ core-shell arrays. *Electrochim. Acta* **2020**, *332*, No. 135433.
(13) Cui, P.; Zhang, P.; Chen, X.; Chen, X.; Wan, T.; Zhou, Y.; Su, M.; Liu, Y.; Xu, H.; Chu, D. Oxygen Defect and Cl−-Doped Modulated $TiNb_2O_7$ Compound with High Rate Performance in Lithium-Ion Batteries. *ACS Appl. Mater. Interfaces* **2023**, *15* (37), 43745−43755.
(14) Zheng, J.; Xia, R.; Sun, C.; Yaqoob, N.; Qiu, Q.; Zhong, L.; Li, Y.; Kaghazchi, P.; Zhao, K.; Elshof, J. E. t.; Huijben, M. Fast and Durable Lithium Storage Enabled by Tuning Entropy in Wadsley−Roth Phase Titanium Niobium Oxides. *Small* **2023**, *19* (30), No. 2301967.
(15) Chang, H.; Wu, Y.-R.; Han, X.; Yi, T.-F. Recent developments in advanced anode materials for lithium-ion batteries. *Energy Materials* **2022**, *1* (1), 100003.
(16) Pham-Cong, D.; Kim, J.; Tran, V. T.; Kim, S. J.; Jeong, S.-Y.; Choi, J.-H.; Cho, C. R. Electrochemical behavior of interconnected $Ti_2Nb_{10}O_{29}$ nanoparticles for high-power Li-ion battery anodes. *Electrochim. Acta* **2017**, *236*, 451−459.
(17) Liu, X.; Liu, M.; Hu, Y.; Hu, M.; Duan, X.; Liu, G.; Ma, J. Mesoporous $Ti_2Nb_{10}O_{29}$ microspheres constructed by interconnected nanoparticles as high performance anode material for lithium ion batteries. *Ceram. Int.* **2019**, *45* (3), 3574−3581.
(18) Oskouei, H. I.; Aghamohammadi, H.; Eslami-Farsani, R. Electrochemical performance of $TiNb_2O_7$ nanoparticles anchored with different contents of MWCNTs as anode materials for Li-ion batteries. *Ceram. Int.* **2022**, *48* (10), 14717−14725.
(19) Yang, C.; Yu, S.; Ma, Y.; Lin, C.; Xu, Z.; Zhao, H.; Wu, S.; Zheng, P.; Zhu, Z.-Z.; Li, J.; Wang, N. $Cr^{3+}$ and $Nb^{5+}$ co-doped $Ti_2Nb_{10}O_{29}$ materials for high-performance lithium-ion storage. *J. Power Sources* **2017**, *360*, 470−479.
(20) Liu, X.; Wang, H.; Zhang, S.; Liu, G.; Xie, H.; Ma, J. Design of well-defined porous $Ti_2Nb_{10}O_{29}$/C microspheres assembled from nanoparticles as anode materials for high-rate lithium ion batteries. *Electrochim. Acta* **2018**, *292*, 759−768.
(21) Wu, Q.; Kang, Y.; Chen, G.; Chen, J.; Chen, M.; Li, W.; Lv, Z.; Yang, H.; Lin, P.; Qiao, Y.; Zhao, J.; Yang, Y. Ultrafast Carbothermal Shock Synthesis of Wadsley−Roth Phase Niobium-Based Oxides for Fast-Charging Lithium-Ion Batteries. *Adv. Funct. Mater.* **2024**, *34* (23), No. 2315248.
(22) Ji, X.; Yang, Y.; Ding, Y.; Lu, Z.; Liu, G.; Liu, Y.; Song, J.; Yang, Z.; Liu, X. Fluorine-Doped Carbon-Coated Mesoporous $Ti_2Nb_{10}O_{29}$ Microspheres as a High-Performance Anode for Lithium-Ion Batteries. *J. Phys. Chem. C* **2022**, *126* (18), 7799−7808.
(23) Deng, S.; Chao, D.; Zhong, Y.; Zeng, Y.; Yao, Z.; Zhan, J.; Wang, Y.; Wang, X.; Lu, X.; Xia, X.; Tu, J. Vertical graphene/$Ti_2Nb_{10}O_{29}$/hydrogen molybdenum bronze composite arrays for enhanced lithium ion storage. *Energy Storage Materials* **2018**, *12*, 137−144.
(24) Zhang, X.; Sun, J.; Cheng, Z.; Wu, M.; Guo, Z.; Zhang, H. Design, Perspective, and Challenge of Niobium-Based Anode Materials for High-Energy Alkali Metal-Ion Batteries. *Adv. Funct. Mater.* **2024**, *34*, No. 2405392.
(25) Cheng, L.-Q.; Xie, X.; Chen, K.; He, Y.; Xu, H.; Liu, R.; Feng, M. Enhancing the electrochemical properties of $TiNb_2O_7$ anodes with SP-CNT binary conductive agents for both liquid and solid state lithium ion batteries. *RSC Adv.* **2024**, *14* (22), 15722−15729.
(26) Deng, Q.; Fu, Y.; Zhu, C.; Yu, Y. Niobium-Based Oxides Toward Advanced Electrochemical Energy Storage: Recent Advances and Challenges. *Small* **2019**, *15* (32), No. 1804884.
(27) Budak, Ö.; Srimuk, P.; Aslan, M.; Shim, H.; Borchardt, L.; Presser, V. Titanium Niobium Oxide $Ti_2Nb_{10}O_{29}$/Carbon Hybrid Electrodes Derived by Mechanochemically Synthesized Carbide for High-Performance Lithium-Ion Batteries. *ChemSusChem* **2021**, *14* (1), 398−407.
(28) Zeng, J.; Yang, L.; Shao, R.; Zhou, L.; Utetiwabo, W.; Wang, S.; Chen, R.; Yang, W. Mesoscopic $Ti_2Nb_{10}O_{29}$ cages comprised of nanorod units as high-rate lithium-ion battery anode. *J. Colloid Interface Sci.* **2021**, *600*, 111−117.
(29) Griffith, K. J.; Harada, Y.; Egusa, S.; Ribas, R. M.; Monteiro, R. S.; Von Dreele, R. B.; Cheetham, A. K.; Cava, R. J.; Grey, C. P.; Goodenough, J. B. Titanium Niobium Oxide: From Discovery to Application in Fast-Charging Lithium-Ion Batteries. *Chem. Mater.* **2021**, *33* (1), 4−18.
(30) Geng, S.; Zhang, Y.; Shi, L.; Shi, A.; Zhou, L.; Kang, C.; Qiang, Z.; Zhu, J.; Dong, S.; Li, D.; Yin, G.; Lou, S. Enabling 20 min fast-charging Ah-level pouch cell by tailoring the electronic structure and ion diffusion in $TiNb_2O_7$. *Energy Storage Materials* **2024**, *68*, No. 103339.
(31) Yao, Z.; Xia, X.; Zhang, Y.; Xie, D.; Ai, C.; Lin, S.; Wang, Y.; Deng, S.; Shen, S.; Wang, X.; Yu, Y.; Tu, J. Superior high-rate lithium-ion storage on $Ti_2Nb_{10}O_{29}$ arrays via synergistic TiC/C skeleton and N-doped carbon shell. *Nano Energy* **2018**, *54*, 304−312.
(32) Deng, S.; Luo, Z.; Liu, Y.; Lou, X.; Lin, C.; Yang, C.; Zhao, H.; Zheng, P.; Sun, Z.; Li, J.; Wang, N.; Wu, H. $Ti_2Nb_{10}O_{29-x}$ mesoporous microspheres as promising anode materials for high-performance lithium-ion batteries. *J. Power Sources* **2017**, *362*, 250−257.
(33) Dong, H.; Chen, X.; Yao, T.; Ge, Q.; Chen, S.; Ma, Z.; Wang, H. Rational design of hollow $Ti_2Nb_{10}O_{29}$ nanospheres towards High-Performance pseudocapacitive Lithium-Ion storage. *J. Colloid Interface Sci.* **2023**, *651*, 919−928.
(34) Wu, X.; Miao, J.; Han, W.; Hu, Y.-S.; Chen, D.; Lee, J.-S.; Kim, J.; Chen, L. Investigation on $Ti_2Nb_{10}O_{29}$ anode material for lithium-ion batteries. *Electrochem. Commun.* **2012**, *25*, 39−42.
(35) Tao, R.; Yang, G.; Self, E. C.; Liang, J.; Dunlap, J. R.; Men, S.; Do-Thanh, C.; Liu, J.; Zhang, Y.; Zhao, S.; Lyu, H.; Sokolov, A. P.; Nanda, J.; Sun, X.; Dai, S. Ionic Liquid-Directed Nanoporous $TiNb_2O_7$ Anodes with Superior Performance for Fast-Rechargeable Lithium-Ion Batteries. *Small* **2020**, *16* (29), No. 2001884.
(36) Liu, J.; Zhao, X.; Duan, L.; Cao, M.; Sun, H.; Shao, J.; Chen, S.; Xie, H.; Chang, X.; Chen, C. Influence of annealing process on conductive properties of Nb-doped $TiO_2$ polycrystalline films


https://doi.org/10.1021/acsomega.5c01447
*ACS Omega* 2025, 10, 15744−15752

prepared by sol−gel method. *Appl. Surf. Sci.* **2011**, *257* (23), 10156−10160.
(37) Yu, G.; Huang, J.; Bai, X.; Li, T.; Song, S.; Zhou, Y.; Wu, N.; Yao, S.; Lu, X.; Wu, W. Engineering of Cerium Modified $TiNb_2O_7$ Nanoparticles For Low-Temperature Lithium-Ion Battery. *Small* **2024**, *20*, No. e2308858.
(38) Yuan, T.; Luo, S.; Soule, L.; Wang, J.-H.; Wang, Y.; Sun, D.; Zhao, B.; Li, W.; Yang, J.; Zheng, S.; Liu, M. A hierarchical $Ti_2Nb_{10}O_{29}$ composite electrode for high-power lithium-ion batteries and capacitors. *Mater. Today* **2021**, *45*, 8−19.
(39) Zhao, Z.; Xue, Z.; Xiong, Q.; Zhang, Y.; Hu, X.; Chi, H.; Qin, H.; Yuan, Y.; Ni, H. Titanium niobium oxides ($TiNb_2O_7$): Design, fabrication and application in energy storage devices. *Sustainable Materials and Technologies* **2021**, *30*, No. e00357.
(40) Yang, Y.; Huang, J.; Cao, Z.; Lv, Z.; Wu, D.; Wen, Z.; Meng, W.; Zeng, J.; Li, C. C.; Zhao, J. Synchronous Manipulation of Ion and Electron Transfer in Wadsley−Roth Phase Ti-Nb Oxides for Fast-Charging Lithium-Ion Batteries. *Adv. Sci.* **2021**, *9* (6), No. 2104530.
(41) Zhang, Y.; Tang, Y.; Liu, L.; Gao, Y.; Zhu, C.; Bai, X.; Wang, X. $TiNb_xO_{2+2.5x}$ ($x$ = 2, 5, 6)/C hybrid nanotubes with enhanced kinetics for high-performance lithium anodes. *Electrochim. Acta* **2022**, *410*, No. 139862.
(42) Zhan, J.; Hu, R.; Luo, X.; Zhang, C.; Luo, G.; Fan, J.; Clark, J. H.; Zhang, S. Highly selective conversion of phenol to cyclohexanol over Ru/$Nb_2O_5$-nC18PA catalysts with increased acidity in a biphasic system under mild conditions. *Green Chem.* **2022**, *24* (3), 1152−1164.
(43) Adhami, T.; Ebrahimi-Kahrizsangi, R.; Bakhsheshi-Rad, H. R.; Majidi, S.; Ghorbanzadeh, M. Effects of Active Material Particles Size Distribution on the Fabrication of $TiNb_2O_7$ Electrode Used in Lithium-Ion Batteries. *J. Adv. Mater. Process.* **2021**, *9* (3), 15−22.
(44) Lu, X.; Jian, Z.; Fang, Z.; Gu, L.; Hu, Y.-S.; Chen, W.; Wang, Z.; Chen, L. Atomic-scale investigation on lithium storage mechanism in $TiNb_2O_7$. *Energy Environ. Sci.* **2011**, *4* (8), 2638−2644.
(45) Yuan, T.; Sun, D.; Sun, Y.; Sun, Y.; Pang, Y.; Yang, J.; Zheng, S. Wearable high power flexible lithium-ion capacitors with adjustable areal loading. *Chemical Engineering Journal* **2023**, *474*, No. 145781.
(46) Yuan, K.; Lin, Y.; Li, X.; Ding, Y.; Yu, P.; Peng, J.; Wang, J.; Liu, H.; Dou, S. High-Safety Anode Materials for Advanced Lithium-Ion Batteries. *Energy Environ. Mater.* **2024**, *7* (5), No. e12759.
(47) Wang, C. H.; Huang, L.; Zhong, Y.; Tong, X. L.; Gu, C. D.; Xia, X. H.; Zhang, L.; Wang, X. L.; Tu, J. P. $Ti_2Nb_{10}O_{29}$ anchored on Aspergillus Oryzae spore carbon skeleton for advanced lithium ion storage. *Sustainable Materials and Technologies* **2021**, *28*, No. e00272.
(48) Li, Y.; Wang, S.; He, Y.-B.; Tang, L.; Kaneti, Y. V.; Lv, W.; Lin, Z.; Li, B.; Yang, Q.-H.; Kang, F. Li-ion and Na-ion transportation and storage properties in various sized $TiO_2$ spheres with hierarchical pores and high tap density. *Journal of Materials Chemistry A* **2017**, *5* (9), 4359−4367.
(49) Zhu, K.; Feng, W.; Xue, Z.; Sun, M.; Wu, S.; Jing, Z.; Yu, Y. In Situ Conformal Carbon Coating for Constructing Hierarchical Mesoporous Titania/Carbon Spheres as High-Rate Lithium-Ion Battery Anodes. *ACS Sustainable Chem. Eng.* **2022**, *10* (33), 10955−10965.


https://doi.org/10.1021/acsomega.5c01447
*ACS Omega* 2025, 10, 15744−15752